Absorptivity measurements during laser powder bed fusion of pure copper with a 1 kW cw green laser

G. Nordet [a,b,*], C. Gorny [b], Y. Mayi [b], J. Daligault [b], M. Dal [b], A. Effernelli [a], E. Blanchet [a], F. Coste [b], P. Peyre [b]

[a] ADDUP, 5 Rue Bleue, 63118 Cébazat, France
[b] PIMM Laboratory, Arts et Métiers Institute of Technology, CNRS, CNAM, HESAM University 151 Bd de l'Hôpital, 75013 Paris, France

ARTICLE INFO

Keywords:
Green laser
Pure copper
Powder bed fusion
Single beads
Absorption rate measure

ABSTRACT

A 1 kW CW green laser source operating at 515 nm was used to investigate the absorptivity of pure copper powder beds and pure copper substrates. Various interaction regimes were considered, ranging from the solid and/or powder layers, to the liquid state and up to the deep penetration keyhole regime. Reflectance measurements were carried out using an Ulbricht integrating sphere during static tests and single L-PBF tracks. For each experiment, absorptivity values were discussed using the real penetration depth observed on cross-section. Absorptivity values were found to be in relatively good agreement with analytical models of the powder bed and the keyhole regime absorptivity. Such results provide useful insight on the use of green wavelengths for the optimization of the L-PBF process on highly reflective and conductive materials like copper.

1. Introduction

Pure copper is a widely used material in the electronics and power production sectors due to its high thermal and electrical conductivity (see Table 1). Corresponding applications usually involve new and complex geometries combined with fully dense materials to enhance conductivity. For such applications, Additive Manufacturing (AM) seems to be an adequate answer to the need for new design. More precisely, the high precision and spatial resolution provided by the Laser Powder Bed Fusion (L-PBF) technique seems particularly adapted to the manufacturing of very complex forms and the reduction of material waste during the process.

However, the reduction of porosity with classical L-PBF conditions is a real technical issue on pure copper due to a combination of high reflectivity under IR irradiation, and high thermal conductivity. Recent L-PBF studies have shown that a maximum 98.5 % density could be reached on pure copper using very high energy density [1] or new building strategies [2]. More precisely, with a near IR monomode fiber laser, the use of an 800 W to 1 kW power is almost mandatory to reach satisfactory densities. Such conditions, usually obtained with high power densities (>2 MW/cm^2) induce a deep keyhole welding mode, which seems to be the only viable regime for stabilizing fusion tracks. For this reason, L-PBF technology still exhibits limitations to obtain fully dense pure copper, because most of the lasers installed on industrial systems are limited to 500–700 W output powers. The main reason is that the infrared laser wavelength (~1.07 μm) used in the L-PBF system is not well absorbed by pure copper (absorptivity = 4–5%), causing several damages on the laser optics due to back reflections and limiting the laser-powder bed energy coupling. Moreover, using excessive energy density seems to be detrimental to the L-PBF process, due to severe spattering effects and melt-pool surface instabilities. A possible way for stabilizing near IR copper welding is to use wobbling (spatial beam oscillations) which conduces to smoother surfaces for similar penetration depths, or dual spot simultaneous irradiation with an outer beam and a core beam, as shown by Punzel [3]. However, the used wobbling frequencies (200–1000 Hz), which are optimized for a welding mode at nearly 0.1 m/s, should be drastically increased for a L-PBF fusion mode at ten times higher scan speeds.

Some solutions have been developed to reduce the energy density needed to create dense parts on highly reflective materials. Among those solutions, changing the material surface to make it more absorbent seems to be the easier one. For instance, Jadhav et al. [4] have shown that a 2 h – 200 °C controlled oxidation of pure copper powder, resulting in a 100 nm oxide layer, allowed obtaining similar built material's density for a 40% lower energy density. A 90 % increase of the powder bed absorptance (from 0.32 to 0.58) was shown to be the key factor for

* Corresponding author at: ADDUP, 5 Rue Bleue, 63118 Cébazat, France.
E-mail address: guillaume.nordet@ensam.eu (G. Nordet).

Table 1
Thermo-physical properties of copper (s = solid, l = liquid) [16].

Properties	Symbol	Value
Density	ρ	(s): 8930 kg/m^3 (27 °C) (l): 7960 kg/m^3 (1130 °C)
Thermal conductivity	K	(s): 400 W/(K.m) (27 °C) (l): 160 W/(K.m) (1130 °C)
Specific heat	C_p	(s): 387 J/(kg.K) (27 °C) (l): 495 J/(kg.K) (1130 °C)
Surface tension	γ	(l): 1.3 N/m (1080 °C) (l): 1.15 N/m (1500 °C)
Viscosity	η	(l): 0.0043 Pa.s (1080 °C) (l): 0.0027 Pa.s (1500 °C)

this improvement. However, even with a modified copper surface, maximum relative densities of L-PBF samples were close to 98 %.

In another publication [5], the same authors demonstrated a similar benefit (reduction of the needed energy) when adding some carbon particles to the copper powder. However, rather low mechanical properties and electrical conductivities (only 39 % IACS) were measured on L-PBF parts obtained with carbon-coated copper powder, mainly due to carbon and oxygen segregation.

Lindstrom et al [6] also have tested successfully nickel and tin coatings carried out with an electrodeposition method. with significant improvements of the densification rate for constant irradiation conditions. This was also attributed to a factor 2 increase of the powder bed absorptance for all the tested conditions.

The second possible means to improve laser-copper energy coupling is to use newly developed high-power laser sources operating in the visible wavelength range. For instance, the use of recent green lasers has already demonstrated a better coupling with copper for welding applications [7]. Indeed, the green wavelength (λ = 532 or 515 nm) is more absorbed by pure copper not only at a solid state but also at a liquid state. Corresponding absorption rates are expected to be comprised between 40 % [8] and 60 % [9] for solid-state versus 25 % and 50 % levels at liquid state. Recently, the very first industrial L-PBF machine using a 500 W green laser was marketed, with very little information available on the system. However, the laser-material coupling during L-PBF fusion with a green laser has never been published up-to-now.

High power blue diode lasers, operating at 450 nm, are also attractive candidates for welding copper, as shown by Hummel [10] on pure copper and Cu-6Sn alloys. The absorptivity of copper is even higher than at 515–530 nm, with up to 80 % values in the conduction welding regime, versus 60 % at 515 nm. However, even if higher powers are already under development, existing blue laser diodes are still limited in terms of brightness and available focused beam diameter, which limits their possible application for L-PBF, requiring higher scanning speeds than conventional laser welding.

The origin of the strong hydrodynamic instabilities observed during copper welding is still the object of controversy. Moreover, such instabilities tend to increase when using highly focused lasers on powder beds. The use of a pulsed laser regime and a dedicated pulse shaping, combined with a green wavelength on pure copper was shown to stabilize weld seams and lower spattering for usual welding conditions at low scan speeds of 0.01 m/s [11].

Even if there is still a lack of data on laser-material interaction for visible wavelengths, and in L-PBF regime, the Ulbricht sphere technique has been reported several times as an efficient way to investigate laser-matter energy coupling on various kinds of metals or alloys in welding regime [10]. Such a time-resolved technique, combined with post-mortem analysis or real-time synchrotron X-ray radiography of fusion tracks [12,13] provides useful information on coupling efficiency near transition regimes or process instabilities for which laser absorptivity sharply increases or decreases. Very recently, Lane et al.[14] and Simonds et al. [15] have also considered this technique for analysing the IR laser absorptance during L-PBF on a In625 and a 316L powder bed together with simultaneous melt-pool monitoring, and correlation with the tracks' stability. However, up to our knowledge, such techniques have never considered a green laser applied on a pure copper powder bed.

In this context, the present study aimed at investigating the laser absorption of pure copper under the L-PBF regime and the resulting dimensions of single L-PBF tracks. A novel 1 kW cw green laser was used as a potentially good candidate for L-PBF applications on pure copper. However, the extensive use of such a laser deserves a precise analysis of laser-powder bed coupling, which is the objective of the current work. At first, the reflectivity R will be estimated for static and dynamic laser irradiations (on plate and L-PBF single tracks) carried out in an Ulbricht integrating sphere. In the second stage, the bead stability and dimensions (width, penetration depth) versus laser power and scan speed will be explored. Combining the two experimental analyses (absorption and bead dimensions) is expected to provide a new and interesting insight onto the interest of green wavelength for L-PBF applications on highly reflective-conductive metals.

2. Experimental setup

2.1. Powder and powder bed

In the present work, a gas-atomized pure copper powder with a size distribution between 15 and 45 μm was used (Fig. 1). The gas-atomized powder was supplied by the Technological University of Belfort-Montbéliard (UTBM). The powder was pre-heated at 70 °C during several days before testing to allow dehydration and favor spreading. For this starting condition, no oxidation could be detected with x-ray measurement (detection limit estimated to 1 % wt %). Pure copper (Cu 99.9 wt %) substrates of 1 mm thickness and 25 mm diameter were then used as a base plate material. The thickness of the manually spread powder bed

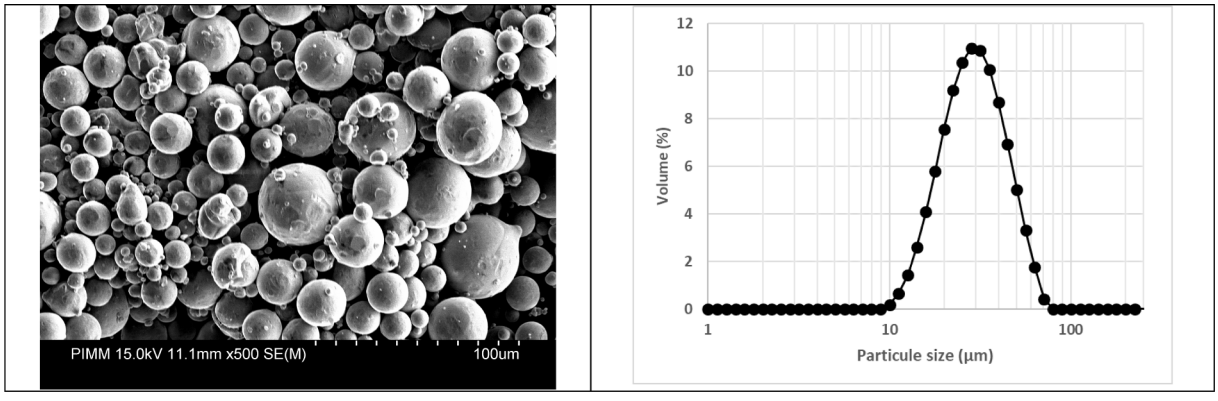

Fig. 1. Left: SEM picture of the copper powder; Right: powder particles distribution.

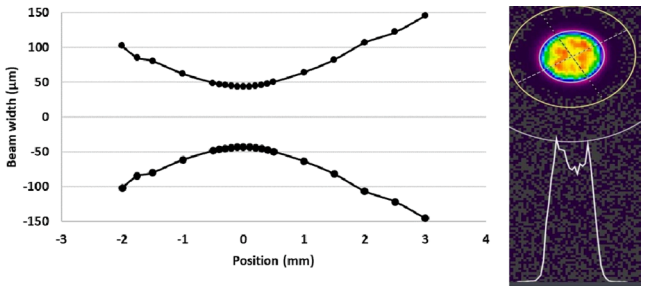

Fig. 2. Beam caustic and beam spot analysed using an Ophir SP928 (camera) equipped with an LBS-300 s attenuator.

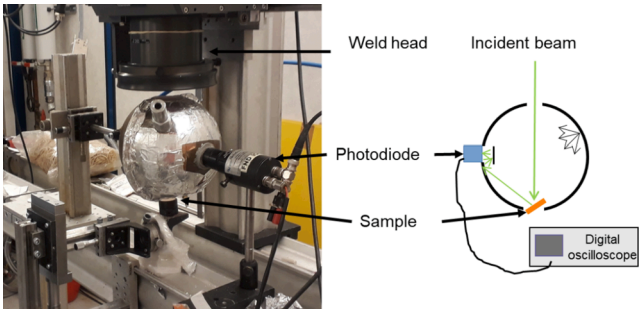

Fig. 3. Image of the experimental setup (left) consisting of the scanner head, the integrating sphere (schematic view on right), the photodiode sensor, and the oscilloscope.

was controlled to 110 ± 10 µm and the powder bed compactness was estimated by mass comparison to 40 ± 5%, which is a relatively low value compared to automatically spread powder beds. To spread out the powder, substrate was put on a Thorlabs tube (as shown in Fig. 3). Then the substrate was lowered down of 110 µm in the tube, controlled by a digital micrometer gauge. Last, the powder was spread out using a razor blade.

2.2. Laser system and reflectivity measurements

Laser tests were performed using a commercial 1 kW CW green laser TruDisk 1020 from Trumpf^{GmbH}, already tested by several authors for welding applications [17] and operating at 515 nm. The focus 168 mm lens allows obtaining a 90 µm top-hat beam (considered at $1/e^2$) at the focal distance (Fig. 2).

Powermeter measurements have been carried out to estimate real ouput powers applied on powder beds. For instance, a 780 W power was measured for a 800 W power set point.

A 160 mm diameter Ulbricht integrating sphere was used for reflectivity R measurements, as already used by Simonds [12] and Allen [13]. Such a setup allows considering all specular and diffusive laser reflections on a prepositioned sample shifted at an 8° angle. The internal side of the sphere was hand-coated with a $BaSO_4$ painting to maximize the reflectance of the sphere. Disk samples of 30 mm diameter and 1 mm thickness were used as substrates. For each analysis, samples were introduced in the sphere with a micrometric guide Table, to control precisely the position between the sample and the laser focal distance. All the shoots have been made in an Ar controlled atmosphere where the oxygen level at the samples is below 2000 ppm.

The intensity of backscattered light on the sphere was measured by a Silicon FND 100 Q photodiode with a band-pass filter to consider only the laser incident wavelength. The output signal was divided by ten using a 100 Ω resistor and a DSO5014A digital oscilloscope was used to record output signals. Fig. 3 shows an image of the experimental setup and a schematic of the integrating sphere.

Two experimental configurations were used:

- Static shoot, to allow a calibration of the photodiode signal vs absorbed laser power with a beam diameter of ~ 500 µm was used.
- Single or multiple fusion tracks with or without powder bed, to address the relationship between laser absorption and resulting final dimensions of tracks. Due to sample inclination and experimental setup, beam diameter various between 140 and 180 µm. The beam diameter is indicated in Table 2 reported as Annex for each track.

Considering laser-copper interaction at this wavelength, the transmittance T was assumed to zero. So, the absorptance A of the surface was directly determined from the measured reflectance R (Eq. (1)).

$$T = 0 \rightarrow A = 1 - R \tag{1}$$

3. Reflectivity measurements

3.1. Photodiode calibration

The photodiode was calibrated by considering the voltage – laser power dependence in solid-state, for two pure metals: aluminium and copper (Cu-ETP 99.9 % Cu), with a similar surface finish obtained with a 1000 SiC paper polishing.

A large beam diameter (500 µm) was used to allow calibration on a large power range, without surface melting (40 W to 480 W on Fig. 4). As illustrated in Fig. 4, a linear dependence is shown between photodiode voltage and incident power below 480 W i.e. in solid-state. Above 480 W, the U = f(P) slope tends to decrease gradually with the occurrence of a fusion regime that corresponds to a higher absorptance of aluminium. Results also indicate a lower reflectivity (i.e. higher absorptance) of copper than aluminium for λ = 515 nm, following literature data [18,20] and less pronounced fusion for copper (Fig. 4a).

Considering that further laser fusion tests will be performed with a smaller laser beam (~150 µm), it must be mentioned here that the amount of collected photons per second n stays the same for an incident beam power, whatever the beam diameter as illustrated by Eq. (2).

$$n = \frac{P\,\lambda}{h\,c} \tag{2}$$

n = number of photons per second, P = laser power (W), λ = wavelength, h = Planck's constant, c = speed of light

Following this calibration stage, all the absorptance values presented later on in the paper were calculated by Eq. (3), considering a reference reflectance value (1-A_{ref}) of aluminium at solid-state equal to 80 ± 10 % [19]. This reference (A_{ref} = 20 ± 10 %) value must be considered with caution because experimental conditions (surface preparation of Al substrate, wavelength of 532 nm instead of 515 nm) were not fully the same than ours. This is why the estimated error bar of ±10% is so high.

$$A_m = 1 - \left(1 - A_{ref}\right)\frac{U_m}{U_{ref}} \tag{3}$$

Where A_m is the measured absorptance, A_{ref} is the reference absorptance taken for the reference material, U_m is the measured tension of the photodiode and U_{ref} is the reference tension of the photodiode measured for the reference material.

3.2. Absorptivity measurement on bead-on-plate and L-PBF tracks

In the current paragraph, all the laser tracks have been carried out on pure copper (substrate and powder), with a variation of speed (0.2, 0.5, 0.8 m/s), of laser power (35 W to 780 W) and beam diameter (140 to 180 µm). The corresponding volume energy density (VED) used in welding models [21,22], or recent L-PBF works is defined by Eq. (4).

$$VED = \frac{4P}{V\pi D^2} \tag{4}$$

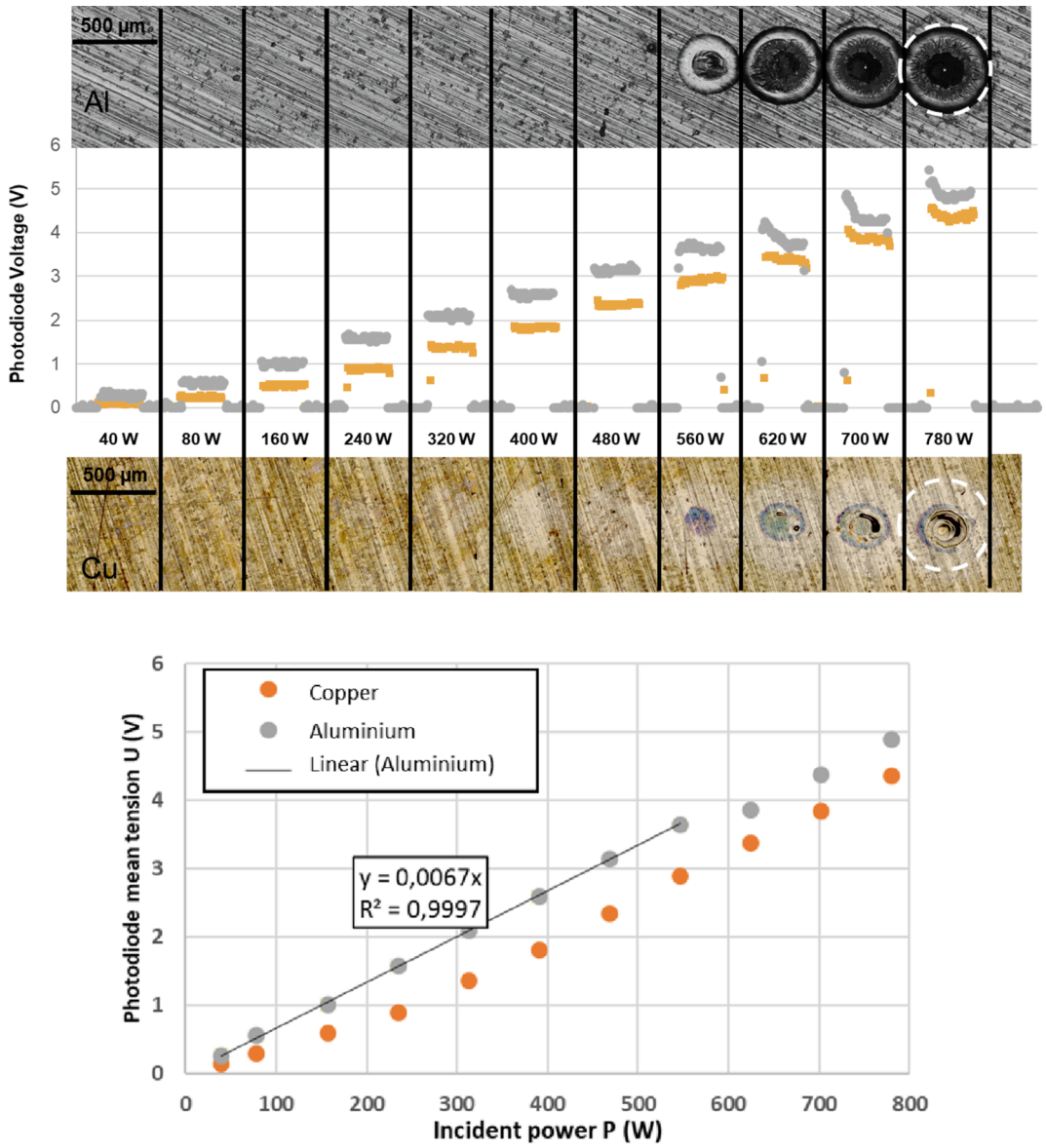

Fig. 4. Calibration of the photodiode signals for static laser shoots (t_{pulse} = 20 ms) and incremental power values (laser spot in white dotted line): (a) experimental signals and corresponding surface aspects, (b) calibration curves (a nonmelt regime is shown up to 480 W on the two metals).

With P = laser power (W), V = scan speed (m/s) and D = laser diameter (m)

The absorption rate was determined for each case using the measured photodiode signal U_m at a frequency of 50,000 samples/s using Eq. (3). To compare the effect of powder on the fusion of a single track, the same laser conditions have been used for bead-on-plate and L-PBF tests.

The absorptance measurement was systematically compared to the surface morphology of the final bead and cross-section analysis of the beads. Such cross-sections were considered at two different locations (respectively 3 mm and 7 mm distant from at the start and the end of the track), and analysed with a Zeiss optical microscope, after a mechanical polishing up to 0.25 µm diamond and a chemical etching (1/3 chloric acid, 2/3 acetic acid, saturated in picric acid). The surface view allowed comparing the bead width to the laser beam diameter. The cross-section allowed evaluating the fusion regime (conduction versus keyhole). All experimental conditions, absorptance data, and melt-pool dimensions are summarized in Table 2 reported as Annex.

Two examples of experimental measurements, corresponding to two different energy conditions are presented in Fig. 5 (P = 468 W, V = 0.5 m/s) and Fig. 6 (P = 780 W, V = 0.5 m/s), for bead-on-plate (a) and L-PBF (b) conditions.

In the first example (Fig. 5), the bead-on-plate fusion (Fig. 5a) is carried out in a conduction regime, corresponding to a smooth bead's surface and a low penetration depth (~50 µm) with near-elliptical shapes on cross-sections. The absorption occurs essentially in a liquid state because the laser diameter (~150 µm) is almost fully included within the bead width. The corresponding absorptance ranges between 16 and 20 %, with rather stable A values with time. For smaller input energies (i.e. lower power or higher speed), the laser absorption would occur on a combination of liquid and solid-state.

Using exactly the same conditions on a 100 µm – thick powder bed (Fig. 5b) provides somewhat different results: (1) the bead is 4 times deeper (195 µm) than without powder (50 µm), (2) the absorption rate measured is higher (around 80 %) and little more unstable versus recording time. Such differences are assumed to be due to the change in welding regime caused by multi-reflection on the keyhole walls, possibly combined with laser trapping in the powder bed on specific non-melted zones. The current 468 W power used in Fig. 5 shows the threshold between the two welding regimes. Powder beds lightly increase

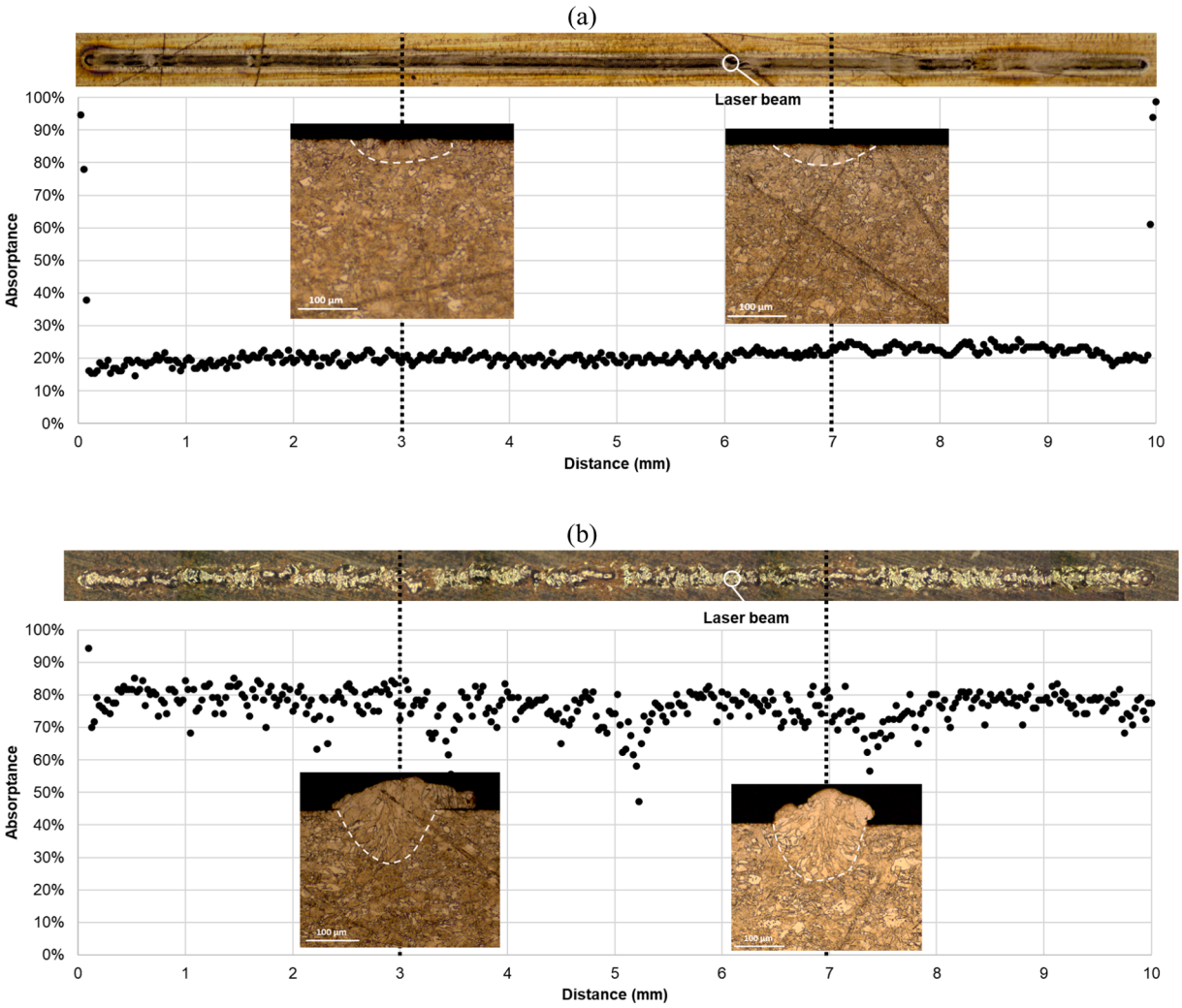

Fig. 5. Absorptivity measurement during (a) a single bead-on-plate fusion track, (b) a single L-PBF track (P = 468 W, V = 0.5 m/s, d = 150 µm, VED = 53 J/mm^3).

absorptance that could allow to easy creation of keyholes. Moreover, that power constitutes a limit between well-continuous tracks and not continuous tracks on the powder bed. This threshold on track's continuity corresponding with the apparition of keyhole on powder bed tracks.

In the second example, due to the higher input power, a higher absorption rate (80 %) and a higher penetration depth (275 µm) are observed on bare substrates (Fig. 6a). In that case, penetration depth/laser diameter aspect ratio is higher (~1.8), and the bead's surface is rougher, which confirms the occurrence of a keyhole regime, involving multi-reflections of the laser on the vapor capillary walls and melt-pool instabilities. In this condition, the bead width (270 µm) is larger than the beam diameter (150 µm), which confirms that most of the absorption has occurred on the keyhole, and not on the surrounding non-deformed liquid.

Using the same conditions on a 100 µm bed powder (Fig. 6b) does not modify significantly the absorptance values (A ~ 0.85) and fusion bead aspects (except the built volume above the substrate).

A compilation of all the absorptance data, either on bare substrates or on powder bed is presented in Fig. 7 for a large range of laser power. The comparison of bead-on-plate and L-PBF data and the variation of absorptance values with laser power both provide an interesting insight. Three power domains are mostly evidenced:

- Below 100 W, the laser-matter interaction occurs on a solid substrate (bead-on-plate) or on the powder bed with multi-reflections on the powder particles. This explains the difference in absorptance (~45 % for solid copper, and 74 % for a solid powder bed)
- Between 100 W and 230 W for the powder bed and 380 W for the copper substrate, absorptance values (bead-on-plate and L-PBF) tend to decrease. This corresponds to the onset of melting and the step-by-step melt-pool enlargement. The laser-matter interaction occurs on a liquid state on the irradiated substrate (A ~ 20 % for the liquid copper), and on a mixture of liquid and powder on powder bed (with A ~ 58 %). This power range is then assumed to generate a conduction welding mode.
- Above 320 W (L-PBF) and 380 W (substrate), the absorptance increases again for both conditions, and tends towards nearly similar values (80 %) at high power. "A similar result was obtained numerically by Khairallah [23] on 316L steel, with a perfect coincidence of absorption on bare plate and powder bed at high intensity". This last condition corresponds to the keyhole regime where laser rays are trapped during multi-reflections on keyhole walls. Finally, it was shown that the corresponding keyhole thresholds, for which the absorptance increases sharply, are lower on the powder bed, due to a ~ 2 times higher absorptance of the powder bed (60 % versus 28 %)

A nearly similar tendency of absorptance versus incident power was obtained by Simonds et al [15] during reflectivity measurements with static IR laser irradiations on a 316L powder bed. However, on copper, the transition from conduction to keyhole welding seems to be steeper

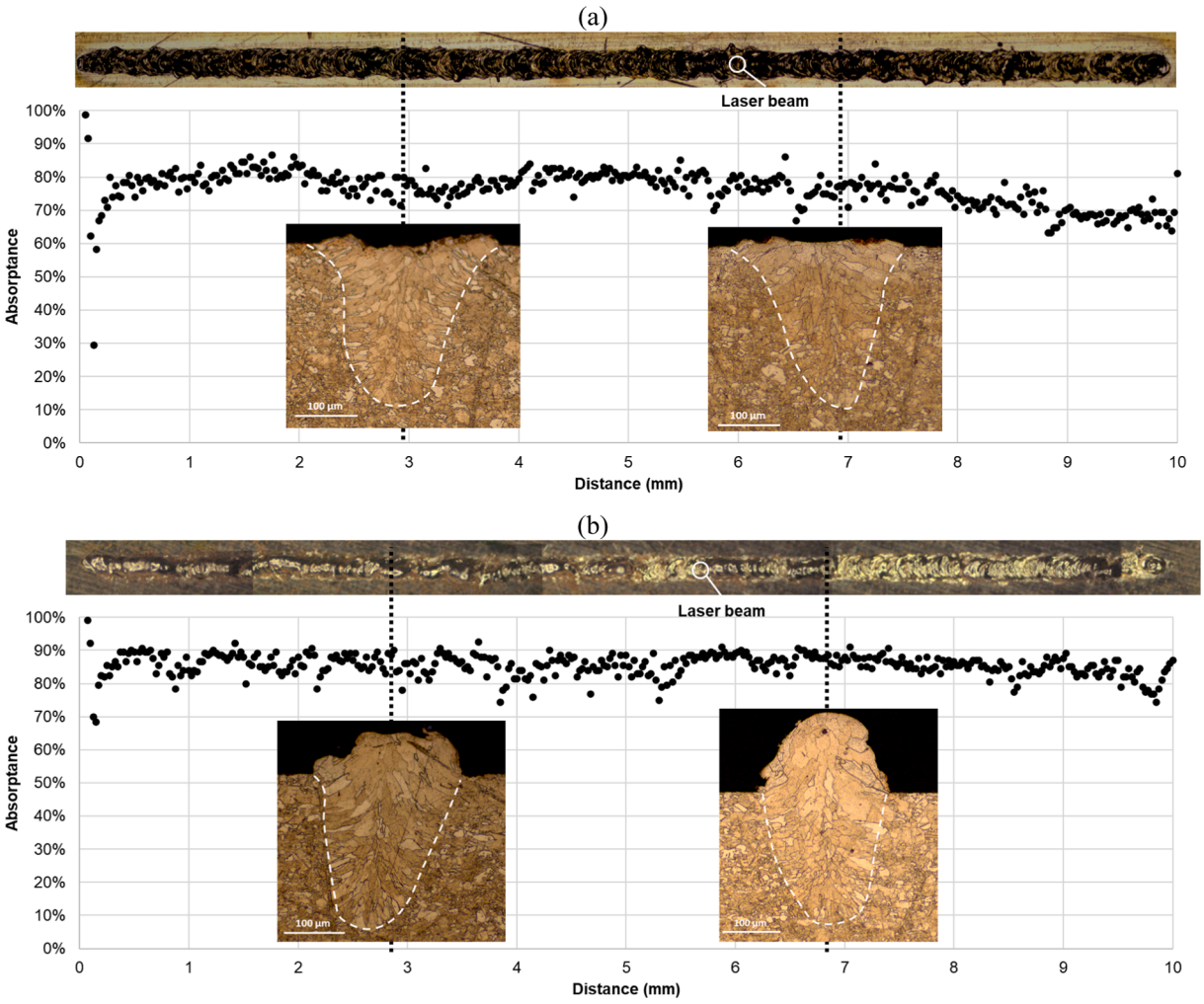

Fig. 6. Absorptivity measurement during (a) a single bead-on-plate fusion track, (b) a single L-PBF track (P = 780 W, V = 0.5 m/s, d = 150 µm, VED = 88 J/mm^3).

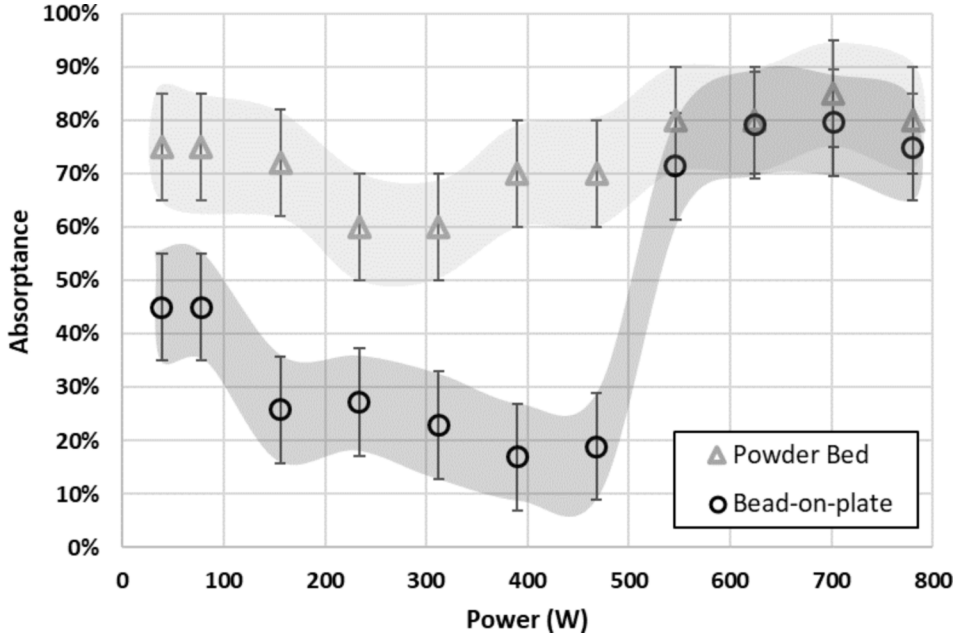

Fig. 7. Measured absorptance versus laser powder for single tracks carried out on powder beds (gray triangles) or bare substrates (black circles). V = 0.2 m/s, d = 180 µm (errors bars come from the reference absorptance value on aluminium +/- 10% and the fluctuation of the absorptance vs time data).

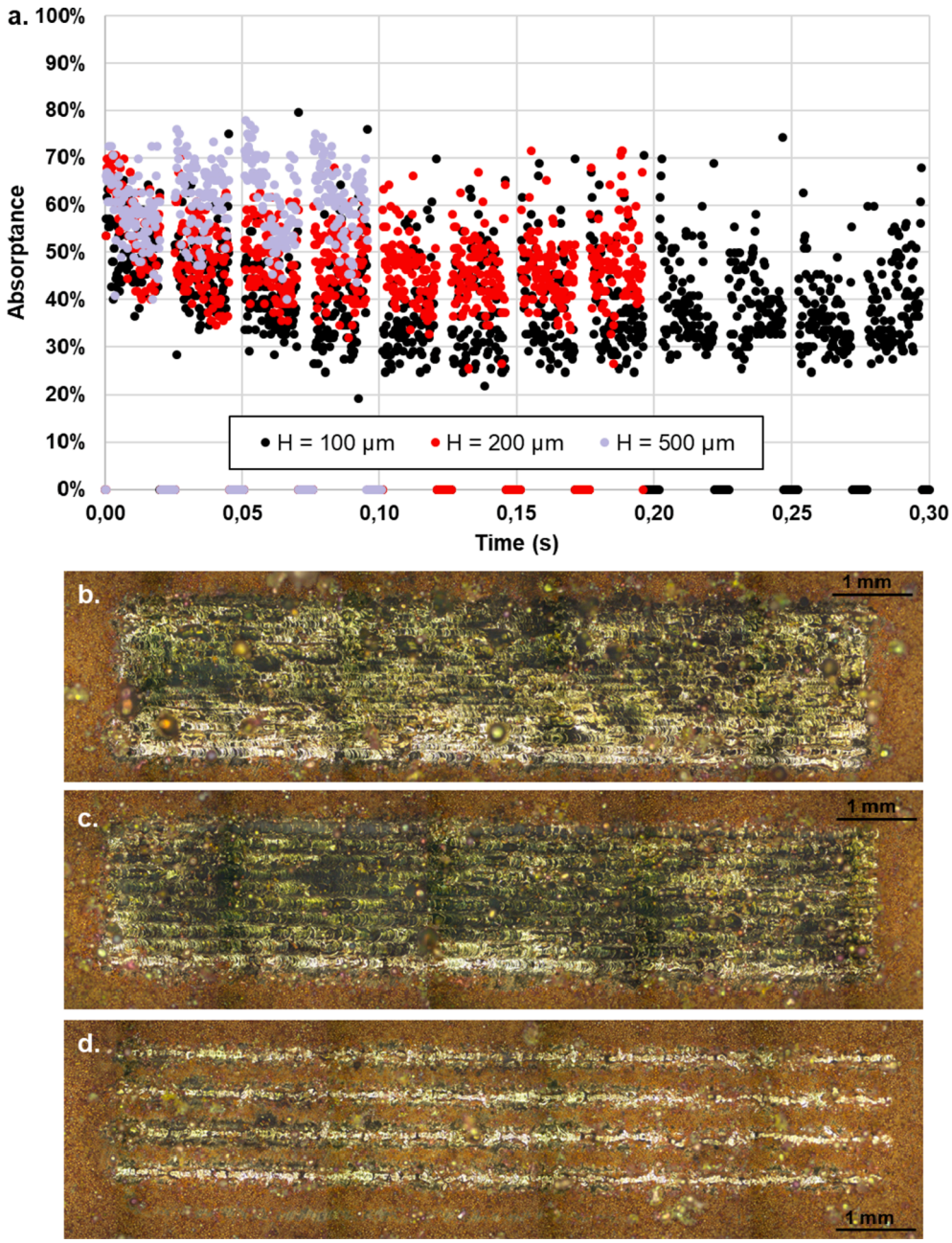

Fig. 8. (a) Absorptance measurement versus time of multiples tracks for three hatches (black: H = 100 µm; red: H = 200 µm; blue: H = 500 µm), (b-c-d) corresponding surface aspect (b: 100 µm; c: 200 µm; d: 500 µm) for P = 468 W, V = 0.5 m/s, d = 150 µm. (For interpretation of the references to colour in this figure legend, the reader is referred to the web version of this article.)

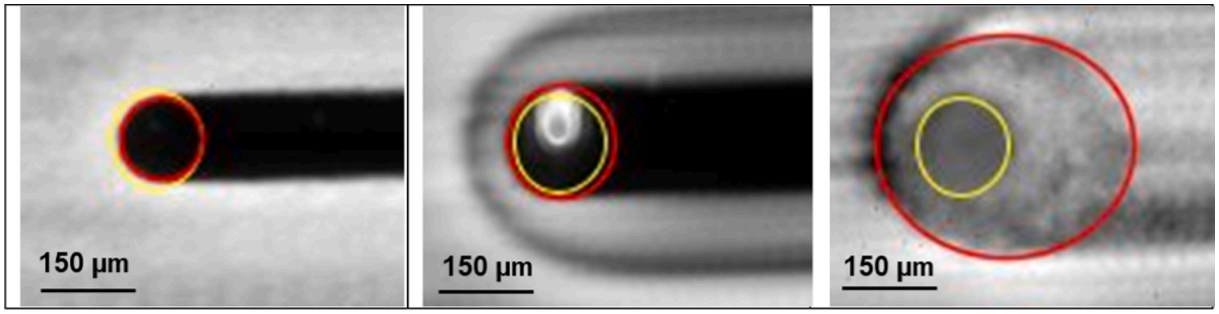

Fig. 9. High speed video (3 kHz) analysis of a bead-on-plate fusion. Left: 234 W – 0.2 m/s Middle: 468 W – 0.2 m/s; Right: 780 W – 0.2 m/s (red = melt-pool contour, yellow = laser). (For interpretation of the references to colour in this figure legend, the reader is referred to the web version of this article.)

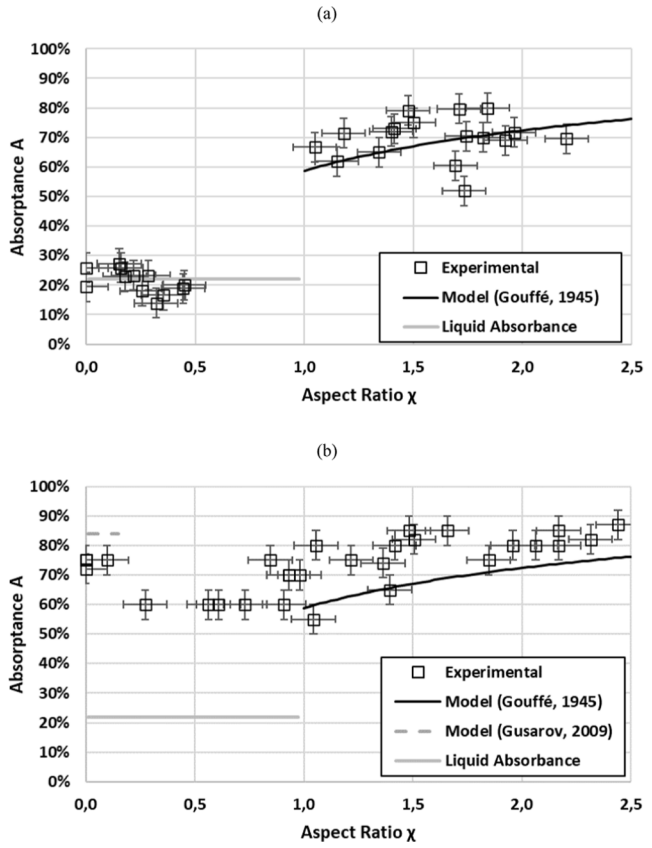

Fig. 10. Comparison of experimental absorptance versus keyhole aspect ratio values (empty square) with geometric models of absorptance. (a) without powder (on bead fusion), (b) with powder (L-PBF).

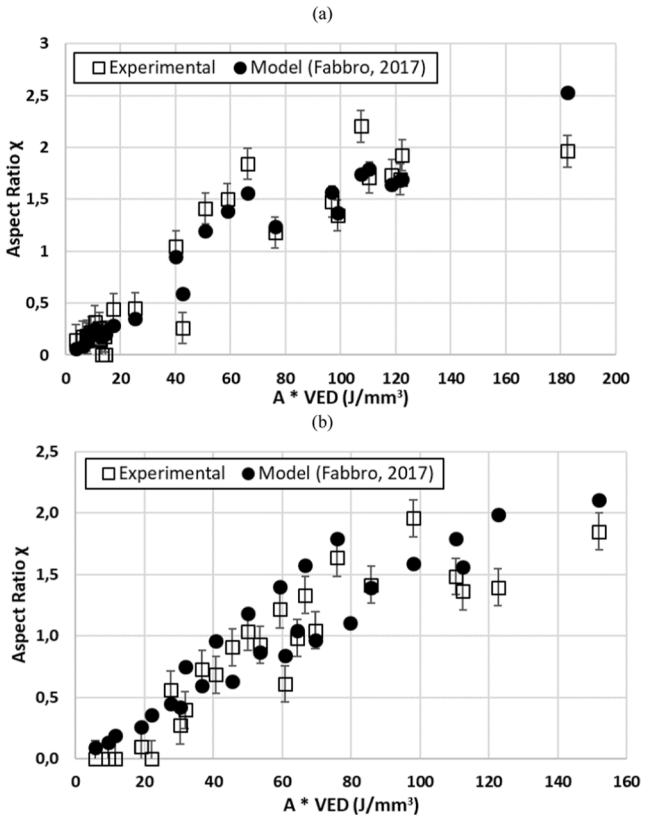

Fig. 11. Experimental (empty square) and model (black circle) (Fabbro, 2017) comparison of the aspect ratio. (a) without powder (on bead fusion), (b) with powder (L-PBF).

Table 3
Comparison of Fabbro's model equation parameters for copper and 316L Steel.

Material	M	N
Copper	24,6 J/mm^3	1.53 W/μm
316L Steel	17.7 J/mm^3	0.21 W/μm

than on 316L stainless steel. Errors bars are quite important due to the variation of the reference value.

Following this experimental work, questions still remain concerning the difference of absorptance between L-PBF and bead-on-plate above 100 W (either in conduction welding regime or in keyhole welding regime) because L-PBF absorptance is always shown to be higher than the absorptance of the substrate. This is particularly obvious between 150 W and 480 W (A ~ 0.65 ± 0.05 versus 0.22 ± 0.05), but also detectable at higher power (A ~ 0.82 versus 0.78 above 480 W). This result could be due to an intermediary regime for which laser interacts with a combination of powder + spheroidized melt pool + underlying solid, starting with the onset of melting, and resulting in a geometrical trapping condition.

Additional questions remain concerning the dynamic behavior of the absorptance during time-resolved tests (Fig. 5, Fig. 6). The fluctuation of reflectivity values seems to be higher on the powder bed than on the bare substrate (Fig. 5b vs Fig. 5a), but also higher near the keyhole threshold. A nearly similar approach by Simonds [15] on a 316L powder bed also evidences time-fluctuating absorptance values during L-PBF in near keyhole welding mode. Such a keyhole instability and resulting absorptance fluctuation is due to the destabilization of the rear keyhole wall, and has been confirmed analytically by Fabbro [24] and numerically by Mayi [25].

4. Analysis of multiple L-PBF tracks – Influence of hatch distance

The optimization of hatch distance (H), i.e. the distance between two consecutive beads, is a major issue in L-PBF, and more specifically on highly conductive materials like copper. Indeed, due to the denudation phenomenon occurring on both edges of the first laser track, the next tracks are supposed to interact either with the powder bed surface or with the denudated area (=the substrate or the last solidified layer). This denudated area has been attributed by Matthews and al. [26] to a recirculation flow dragging powder particles towards laser-induced melt-pool. In the current work, three different hatch distances (100 μm, 200 μm, 500 μm) are considered to create a 10 mm length × 2 mm width L-PBF surface:

- The 100 μm hatch distance (=67 % laser diameter) corresponds to a 50 % overlap between adjacent beads. In that case, laser-matter interaction occurs both on the preview bead and the denudated area.
- With a 200 μm hatch distance, a 5 % overlap is shown between adjacent beads. Laser matter interaction partly occurs on the denudated area and in the powder bed.
- With a 500 μm hatch, laser-matter interaction occurs fully on the powder bed, with no expected impact of the previous bead.

For all three conditions, laser power, scan speed and beam diameter are kept constant: P = 468 W, V = 0.5 m/s, d = 150 μm. Fig. 8 shows the variation of the measured absorptance versus time for the three hatch distances and the resulting surface aspects.

Absorptance data show that:

- For each fusion track (time duration = 20 ms), the absorptance strongly fluctuates and ranges between a minimum and a maximum value (for instance between 25 % and 50 % for H = 100 μm). This fluctuation is rather higher than previous results on single L-PBF tracks (Fig. 4b and Fig. 5b) and could be explained by the extensive formation of spatters and metal vapor absorbing part of the incident laser light during multi-scan L-PBF. Such time-resolved absorptance variations should be different from those occurring in a real L-PBF machine where a lateral gas flow cleans the atmosphere above the laser-melt-pool interaction zone. Another possible contribution for the time variations of the absorptance can also be due to the inherent keyhole instability near the keyhole threshold (approximately when the keyhole depth = laser diameter), as indicated by Simonds [12], Fabbro [24] and Mayi [25]
- Absorptance increases with an increase of hatch distance (25–50 % with H = 100 μm, 35–55 % with H = 200 μm, and 50–75 % with H = 500 μm). That indicated absorptance decreases when the laser interacts on the denudated area and/or on the last fusion bead.
- The higher and more stable absorptance values are obtained when laser interaction occurs on the powder bed.

Such measurements highlight a clear difference of laser-matter interaction during L-PBF on copper, depending on the position of the laser related to the last bead and denudated area.

5. Discussion

5.1. Absorption data in liquid state: Analysis of high-speed videos

To provide additional insight on absorption data in liquid regime (equivalent to the intermediary regime of Fig. 7) and the transition from solid to a liquid state, one interesting question concerns the real position of laser beam compared to the melt-pool in a highly conductive metal like copper. For a deeper understanding, coaxial high-speed videos were recorded for different laser irradiations. In a preliminary experiment, a short static irradiation was first carried out and positioned precisely in the x,y window of the C-MOS camera sensor to locate precisely the position of the laser spot. In the test-bench, the laser spot is fixed, and it is the sample which move under the spot. The position of the laser spot stays the same on all videos cause laser spot and camera do not move.

At low power and high speed (low VED, Fig. 8a), the laser is not totally contained in the melt pool. In that case, approximately 15 % of the incident laser beam is absorbed by the solid. For higher input energies (Fig. 9b,c), the melt pool remains circular and the laser is fully contained in the melt pool, and the laser absorption occurs only at a liquid state. Such a simple bead-on-plate experiment allows understanding that on copper, due to the high thermal conductivity, the influence of convection flow on melt-pool dimensions is limited, which explains why melt-pool is mostly circular. The effect is that for low VED conditions, the absorption can occur in both liquid and solid states. This is supposed to explain the decrease of absorption data on bare substrates between 100 and 400 W incident power (Fig. 7). For instance, between 234 W and 400 W, the absorptance decreases (from ~ 25 % to 18 %), which corresponds to the transition of absorptance towards a full laser-liquid state interaction (Fig. 9a to Fig. 9b), whereas in Fig. 9a (234 W), the laser is partially absorbed on the solid.

5.2. Absorption data for low and high-energy domains

For estimating the variation of laser absorptance on powder beds, the 2009 model of Gusarov et al. [27] was considered to describe the absorptance of powder in solid-state (Eq. (5)).

$$A = \frac{R\,a}{(4R-3)D_1}\left\{2\left(1-R^2\right)e^{-\lambda} - \left(3+R\,e^{-2\lambda}\right)\times\left\{\left[1+a-R(1-a)\right]e^{2a\lambda} + \left[1-a-R(1+a)\right]e^{-2a\lambda}\right\}\right\} - \frac{3(1-R)(1-R\,e^{-2\lambda})}{4R-3} \quad (5)$$

Where D is defined as:

$$D_1 = (1-a)\left[1-a-R(1+a)\right]e^{-2a\lambda} - (1+a)\left[1+a-R(1-a)\right]e^{2a\lambda}$$

And λ is defined as:

$$\lambda = \frac{3}{2}\frac{1-\varepsilon}{\varepsilon}\frac{L}{D}$$

with

R is the reflectance of the powder material at solid-state in dense form, a is defined as a function of R: $a = \sqrt{1-R}$ *, λ is the optical thickness defined from the diameter of powder (30 μm) and the porosity* ε, L *is the powder bed thickness (110 μm here), and ε is the porosity of powder bed (55 %). From these values, an adimensioned λ value of 3.7 was calculated with D the mean powder diameter and L the powder thickness.*

For low aspects ratio (<0.1–0.2) assumed to correspond to a near solid state regime involving laser light trapping in a powder bed, Gusarov's model slightly overestimates absorptance data (84 % versus 75 %) (Fig. 10b). However, this model was mainly defined for deep powder layers whereas our experimental conditions involve thinner powder beds, equivalent to 3–4 powder particles. Moreover, this model does not consider the fusion of powder which could be observed on our single tracks. This model seems to be good only at the beginning of the melting process. The multi-reflexion process on powder bed described by Gusarov, 2009 can offer a good answered at the observed increased of absorptance on powder bed compared to bead-on-plate measurements at same experimental condition.

Measurements (Fig. 7) clearly indicate an increase in absorptance when a keyhole is created. Recent studies [12,13,28] show a similar increase of absorptance for other materials and using an IR laser. Other works [24,29] have considered already a model of multi-reflection of rays on a black body proposed by Gouffé [30], and considering the influence of the black body aspect ratio χ i.e. of the keyhole aspect ratio (χ = keyhole depth e/laser diameter d).

In this geometrical model, considering the keyhole as a cylinder, two regimes can be distinguished: (1) for $\chi < 1$, the absorption occurs on the liquid surface i.e. in conduction regime, (2). For aspect ratio $\chi > 1$, the absorption occurs on the black body walls i.e. on the keyhole walls and the global absorptance A can be modelled with Eq. (6).

$$\chi < 1 : A = A_0$$

$$\chi > 1 : A = \frac{A_0}{A_0\left(1-\frac{s}{S}\right)+\frac{s}{S}}\left(1+\left(\frac{s}{S}-\frac{s}{S_0}\right)(1-A_0)\right)$$

$$\rightarrow A = \frac{A_0}{A_0(2+4\chi)+1-A_0}\left(2+4\chi-\frac{1}{2\chi}(1-A_0)\right) \quad (6)$$

With $s = \frac{\pi d^2}{4}$ = surface of the incident beam = top surface of the representative cylinder for a cylinder of diameter d and depth e.

$S = \frac{\pi d^2}{2} + \pi de$ = the total surface of the key-hole - cylinder

$S_0 = \pi e^2$ = the surface of an equivalent sphere, with a diameter equal to the key-hole depth.

Using eq.6 and considering the absorptance A_0 of liquid copper ($A_0 \sim 20$ %) allows obtaining the absorptance values (Fig. 10a) for bead-on-plate fusion tracks, in comparison with experimental data, and considering the real penetration depths to estimate the aspect ratio χ. With such assumptions, the Gouffé geometrical model provides A values ranging between 60 % and 75 %, which are 5–10 % lower than experimental data.

In L-PBF, the model underestimates more clearly (~15–20 %) absorptance values (Fig. 10b).

Two explanations are possible for this result:

- An increase of the absorptance on powder bed due to the ejected powder (spatters) interacting with the laser. The interaction of spatters with the incident laser light would then increase the total power absorbed by the system, even in single-track configuration.
- The choice of a cylinder for representing the keyhole geometry. This geometry is assumed to correspond to a lower limit of keyhole absorption.

Last, it must be mentioned that for similar scan speeds and laser diameter, the keyhole thresholds values, for which $\times > 1$, were found to be slightly lower on powder beds than on bare copper substrates. For instance, for V = 0.2 m/s and d = 150 μm (see annexe 1), x aspect ratios above 1 are obtained for P > 500 W on copper substrates, and for P > 450 W on powder beds.

5.3. Calculation of penetration depths using a welding model

Combining the experimental penetration depths obtained with a green laser source, and the determination of laser absorptance of the liquid copper allows using already existing welding models. Among the recent analytical models [21], Fabbro's 2017 approach [22] allows calculating the aspect ratio χ from experimental (P, V, d) input parameters, and thermophysical properties of the target materials (Peclet number, thermal conductivity, vaporization temperature). In this model, the aspect ratio could be estimated using Eq. (7) here below.

$$\chi = \frac{e}{d} = \frac{A(\chi)P}{\mathrm{d}K(T_V - T_0)g(Pe)} \tag{7}$$

Where K = thermal conductivity of liquid copper, Pe is the Peclet number given by $Pe = \frac{Vd}{2\kappa}$ and $g(Pe) = mPe + n$ is a linear function where m and n are experimental data worth m = 4.3 and n = 1.5. This equation was re-written as Eq. (8), where the aspect ratio χ follows a quasi-linear dependence on VED. However, an additional contribution of power is shown by the second term of Eq. (8). This contribution, traduced by N term, is more important for copper than for less conductive materials. Corresponding values of M and N for copper and 316L steel are given in Table 3.

$$\frac{1}{\chi} = M\frac{1}{AVED} + N\frac{d}{AP} \tag{8}$$

With $M = m\rho C_P(T_V - T_0)$ and $N = nK(T_V - T_0)$

Finally, considering the absorbed power in the VED calculation (Fig. 11), the welding model allows a good prediction of aspect ratios on a large range of incident energy densities VED, either in conduction regime (<40 J/mm^3) or in keyhole mode for bead-on-plate tracks (Fig. 11a). The model overestimates the aspect ratio for powder bed tracks (Fig. 11b). A possible way to explain this overestimation stay on the influence of spatters on the measure of reflectance. Indeed, a part of the laser energy could be absorbed by spatters formed by powder passing under the laser. The energy absorbed by the melt-pool at the laser-tracks interface should be lower than the measure one. Using Gouffé's model offer a lower value for absorptance of the keyhole for powder bed and better the aspect ratio estimation using Fabbro's model on powder bed.

Using eq.7, from Fabbro et al. [24] shows that the stability of a single track depends on the ratio between the aspect ratio and absorptance. Compared with IR results from Fabbro, [24], the use of a green laser source allows reducing instability during key-hole formation on copper. For powder bed tracks, the two slopes are closer. So, a keyhole seems to initiate easily on a powder bed and remain rather stable when created. One can add that the formation of a continuous bead on powder seems to have coincided with the occurrence of a keyhole. Finally, powder bed tracks on copper are either continuous when a keyhole is formed or discontinuous i.e. only balling formation, below the keyhole threshold.

6. Conclusion

A detailed analysis of green laser-pure copper absorption was made using time-resolved integrating sphere absorptance measurements for both single tracks and surfaces. The copper absorptance of 515 nm wavelength was measured for some different states (powder bed, liquid, and keyhole). On single tracks, clear changes of absorptance were demonstrated, depending on the fusion regime and on the materials nature (powder bed or bare substrate):

- On bead-on-plate, the absorptance evolve with temperature from an average 45% at solid state to an average 20% on heat conduction state. When a keyhole was created, the absorptance increased due to multiple reflexions on the keyhole walls to an average 70–80% value.
- When interaction occurred on a copper powder-bed, the absorptance varied from 75% without fusion, to 50% at a liquid state and up to 80–90% in key-hole regime.

Such data were compared with fusion bead morphologies and combined with several analytical approaches. Those analytical approaches fitted rather correctly the variation of absorptance measured. Using those approaches, provided a better insight into the laser-copper interaction and the real potential of high-power CW green laser for the L-PBF of copper parts.

Finally, the analysis of multiple tracks showed a clear influence of the denudation with a reduction of absorptance in denudated areas where geometrical trapping is not efficient anymore. On juxtaposed tracks, a stronger fluctuation of instantaneous absorptance values was shown, attributed to the shadowing effect of spatters on laser absorption.

CRediT authorship contribution statement

G. Nordet: Conceptualization, Methodology, Validation, Formal analysis, Investigation, Writing – original draft, Writing – review & editing. **C. Gorny:** Conceptualization, Investigation, Resources, Writing – original draft, Writing – review & editing. **Y. Mayi:** Software, Methodology, Validation, Formal analysis, Resources. **J. Daligault:** Software,

Methodology, Validation, Formal analysis, Resources. **M. Dal:** Software, Methodology, Validation, Formal analysis, Resources. **A. Effernelli:** Conceptualization, Supervision, Project administration, Funding acquisition. **E. Blanchet:** Conceptualization, Validation, Supervision. **F. Coste:** Conceptualization, Software, Investigation, Resources, Funding acquisition. **P. Peyre:** Conceptualization, Methodology, Validation, Formal analysis, Resources, Writing – original draft, Writing – review & editing, Supervision, Project administration, Funding acquisition.

Declaration of Competing Interest

The authors declare that they have no known competing financial interests or personal relationships that could have appeared to influence the work reported in this paper.

Acknowledgement

The authors will thank all the people of PIMM laboratories and AddUp for their help and advice on the work. This work is carried out as part of the Ambition FUI project supported by BPI and Auvergne-Rhˆone- Alpes and Ile-de-France region.

Appendix

See Table 2.

Annexe 1

Bead dimensions and absorptance data versus process conditions (BoP = Bead-on-Plate and PB = Powder-Bed) – n.m. = not measurable.

P (W)	d (μm)	V (m/s)	VED (J/mm^3)	BoP or PB	Depth e (μm)	Aspect ratio χ = e/d	A	A*VED (J/mm^3)
39	180	0.2	8	BoP	26	0.14	45%	3
78	180	0.2	15	BoP	34	0.19	45%	7
156	180	0.2	31	BoP	29	0.16	26%	8
234	180	0.2	46	BoP	27	0.15	27%	13
312	180	0.2	61	BoP	32	0.18	23%	14
390	180	0.2	77	BoP	46	0.26	18%	14
468	180	0.2	92	BoP	80	0.44	19%	17
546	180	0.2	107	BoP	213	1.18	71%	77
624	180	0.2	123	BoP	266	1.48	79%	97
702	180	0.2	138	BoP	308	1.71	80%	110
780	180	0.2	153	BoP	397	2.20	75%	115
39	140	0.2	13	BoP	25	0.18	45%	6
78	140	0.2	25	BoP	20	0.14	45%	11
156	140	0.2	51	BoP	n.m.	n.m.	26%	13
234	140	0.2	76	BoP	n.m.	n.m.	19%	15
390	140	0.2	127	BoP	63	0.45	17%	21
468	140	0.2	152	BoP	188	1.34	65%	99
546	140	0.2	177	BoP	269	1.92	69%	122
780	140	0.2	253	BoP	275	1.96	72%	182
390	150	0.5	44	BoP	33	0.22	20%	9
468	150	0.5	53	BoP	48	0.32	18%	10
546	150	0.5	62	BoP	157	1.05	67%	41
624	150	0.5	71	BoP	212	1.41	73%	51
702	150	0.5	79	BoP	225	1.50	75%	60
780	150	0.5	88	BoP	276	1.84	80%	71
39	180	0.2	8	PB	n.m.	n.m.	75%	6
78	180	0.2	15	PB	n.m.	n.m.	75%	11
156	180	0.2	31	PB	n.m.	n.m.	72%	22
234	180	0.2	46	PB	101	0.56	60%	28
312	180	0.2	61	PB	131	0.73	60%	37
390	180	0.2	77	PB	167	0.93	70%	54
468	180	0.2	92	PB	177	0.98	70%	64
546	180	0.2	107	PB	255	1.42	80%	86
624	180	0.2	123	PB	352	1.96	80%	98
702	180	0.2	138	PB	346	1.96	85%	117
780	180	0.2	153	PB	247	1.37	85%	130
39	140	0.2	13	PB	n.m.	n.m.	75%	10
78	140	0.2	25	PB	14	0.10	75%	19
156	140	0.2	51	PB	38	0.27	60%	30
234	140	0.2	76	PB	127	0.91	60%	46
312	140	0.2	101	PB	85	0.61	60%	61
390	140	0.2	127	PB	146	1.04	55%	70
468	140	0.2	152	PB	191	1.36	74%	112
624	140	0.2	203	PB	259	1.85	75%	152
390	150	0.5	44	PB	127	0.85	75%	33
468	150	0.5	53	PB	158	1.06	80%	42
546	150	0.5	62	PB	226	1.51	82%	51
624	150	0.5	71	PB	222	1.48	85%	60
702	150	0.5	79	PB	249	1.66	85%	68

References

[1] S.D. Jadhav, S. Dadbakhsh, L. Goossens, J.-P. Kruth, J. Van Humbeeck, K. Vanmeensel, Influence of selective laser melting process parameters on texture evolution in pure copper, J. Mater. Process. Technol. 270 (Aug. 2019) 47–58, https://doi.org/10.1016/j.jmatprotec.2019.02.022.

[2] M. Colopi, A.G. Demir, L. Caprio, B. Previtali, Limits and solutions in processing pure Cu via selective laser melting using a high-power single-mode fiber laser, Int. J. Adv. Manuf. Technol. 104 (5–8) (Oct. 2019) 2473–2486, https://doi.org/10.1007/s00170-019-04015-3.

[3] E. Punzel, F. Hugger, R. Dörringer, T.L. Dinkelbach, A. Bürger, Comparison of different system technologies for continuous-wave laser beam welding of copper, Procedia CIRP 94 (2020) 587–591, https://doi.org/10.1016/j.procir.2020.09.081.

[4] S. D. Jadhav, J. Vleugels, J. Kruth, J. Van Humbeeck, and K. Vanmeensel, Mechanical and electrical properties of selective laser-melted parts produced from

surface-oxidized copper powder, *Mater. Des. Process. Commun.*, vol. 2, no. 2, Apr. 2020, doi: 10.1002/mdp2.94.
[5] Jadhav, et al., Influence of Carbon Nanoparticle Addition (and Impurities) on Selective Laser Melting of Pure Copper, Materials 12 (15) (Aug. 2019) 2469, https://doi.org/10.3390/ma12152469.
[6] V. Lindström, et al., Laser Powder Bed Fusion of Metal Coated Copper Powders, Materials 13 (16) (Aug. 2020) 3493, https://doi.org/10.3390/ma13163493.
[7] A. Heider, A. Hess, R. Weber, and T. Graf, Stabilized copper welding by using power modulated green and IR laser beams, in *International Congress on Applications of Lasers & Electro-Optics*, Orlando, Florida, USA, 2011, pp. 395–402. doi: 10.2351/1.5062263.
[8] S. Engler, R. Ramsayer, and R. Poprawe, Process Studies on Laser Welding of Copper with Brilliant Green and Infrared Lasers, *Phys. Procedia*, vol. 12, pp. 339–346, 2011, doi: 10.1016/j.phpro.2011.03.142.
[9] W.-S. Chung, A. Olowinsky, A. Gillner, Process studies on copper laser beam welding over gap by using disc laser at green wavelength, J. Adv. Join. Process. 1 (Mar. 2020), 100009, https://doi.org/10.1016/j.jajp.2020.100009.
[10] M. Hummel, C. Schöler, A. Häusler, A. Gillner, R. Poprawe, New approaches on laser micro welding of copper by using a laser beam source with a wavelength of 450 nm, J. Adv. Join. Process. 1 (Mar. 2020), 100012, https://doi.org/10.1016/j.jajp.2020.100012.
[11] L. Hijazi, E. Kaiser, S. Altarazi, Pulsed green laser welding of copper materials: A statistical-based methodology for parameters setting, Procedia Manuf. 51 (2020) 890–896, https://doi.org/10.1016/j.promfg.2020.10.125.
[12] B.J. Simonds, et al., Simultaneous high-speed x-ray transmission imaging and absolute dynamic absorptance measurements during high-power laser-metal processing, Procedia CIRP 94 (2020) 775–779, https://doi.org/10.1016/j.procir.2020.09.135.
[13] T.R. Allen, W. Huang, J.R. Tanner, W. Tan, J.M. Fraser, B.J. Simonds, Energy-Coupling Mechanisms Revealed through Simultaneous Keyhole Depth and Absorptance Measurements during Laser-Metal Processing, Phys. Rev. Appl. 13 (6) (Jun. 2020), 064070, https://doi.org/10.1103/PhysRevApplied.13.064070.
[14] B. Lane, Transient Laser Energy Absorption, Co-axial Melt Pool Monitoring, and Relationship to Melt Pool Morphology, Addit. Manuf. (2020) 13.
[15] B. J. Simonds, E. J. Garboczi, T. A. Palmer, and P. A. Williams, Dynamic Laser Absorptance Measured in a Geometrically Characterized Stainless-Steel Powder Layer, p. 15, 2020.
[16] K.C. Mills, Recommended values of thermophysical properties for selected commercial alloys, Woodhead, Cambridge, 2002.
[17] E. Kaiser, E.-M. Dold, A. Killi, and S. Zaske, Application benefits of welding copper with a 1 kW, 515 nm continuous wave laser, p. 6.
[18] M.F. Osorio, A. Salazar, F. Prieto, P. Boulanger, P. Figueroa, Three-dimensional digitization of highly reflective and transparent objects using multi-wavelength range sensing, Mach. Vis. Appl. 23 (4) (Jul. 2012) 761–772, https://doi.org/10.1007/s00138-010-0308-6.
[19] H. Kwon, J.J. Yoh, Polarized reflectance of aluminum and nickel to 532, 355 and 266nm Nd:YAG laser beams for varying surface finish, Opt. Laser Technol. 44 (6) (Sep. 2012) 1823–1828, https://doi.org/10.1016/j.optlastec.2012.02.014.
[20] S. Babar, J.H. Weaver, Optical constants of Cu, Ag, and Au revisited, Appl. Opt. 54 (3) (Jan. 2015) 477, https://doi.org/10.1364/AO.54.000477.
[21] A.M. Rubenchik, W.E. King, S.S. Wu, Scaling laws for the additive manufacturing, J. Mater. Process. Technol. 257 (Jul. 2018) 234–243, https://doi.org/10.1016/j.jmatprotec.2018.02.034.
[22] R. Fabbro, M. Dal, P. Peyre, F. Coste, M. Schneider, V. Gunenthiram, Analysis and possible estimation of keyhole depths evolution, using laser operating parameters and material properties, J. Laser Appl. 30 (3) (Aug. 2018), 032410, https://doi.org/10.2351/1.5040624.
[23] S.A. Khairallah, et al., Controlling interdependent meso-nanosecond dynamics and defect generation in metal 3D printing, Science 368 (6491) (May 2020) 660–665, https://doi.org/10.1126/science.aay7830.
[24] R. Fabbro, Depth Dependence and Keyhole Stability at Threshold, for Different Laser Welding Regimes, Appl. Sci. 10 (4) (Feb. 2020) 1487, https://doi.org/10.3390/app10041487.
[25] Y. Mayi *et al.*, Transient dynamics and stability of keyhole at threshold investigated by finite element modeling, p. 11.
[26] M. J. Matthews, Denudation of metal powder layers in laser powder bed fusion processes, *Acta Mater.*, p. 10, 2016.
[27] A.V. Gusarov, I. Yadroitsev, P.h. Bertrand, I. Smurov, Model of Radiation and Heat Transfer in Laser-Powder Interaction Zone at Selective Laser Melting, J. Heat Transf. 131 (7) (Jul. 2009), 072101, https://doi.org/10.1115/1.3109245.
[28] J. Trapp, In situ absorptivity measurements of metallic powders during laser powder-bed fusion additive manufacturing, Appl. Mater. Today (2017) 9.
[29] F. Fetzer, P. Stritt, P. Berger, R. Weber, T. Graf, Fast numerical method to predict the depth of laser welding, J. Laser Appl. 29 (2) (May 2017), 022012, https://doi.org/10.2351/1.4983152.
[30] A. Gouffé, Corrections d'ouverture des corps-noirs artificiels compte tenu des diffusions multiples internes, *Rev. Opt. Théorique Instrum.*, no. 1–3, 1945.